Primary Condensation Rate and Column Relative Humidity as Two Useful Supplements to Atmospheric River Analysis

Ruping Mo[1], Rita So[1], Melinda M. Brugman[1], Curtis Mooney[2], Anthony Q. Liu[2], Matthias Jakob[3], Armel Castellan[4], and Roxanne Vingarzan[5]

[1]National Laboratory-West, Environment and Climate Change Canada, Vancouver, BC, Canada
[2]National Laboratory-West, Environment and Climate Change Canada, Edmonton, Alberta, Canada
[3]BGC Engineering, Vancouver, BC, Canada
[4]Client Services, PSOW, Environment and Climate Change Canada, Victoria, BC, Canada
[5]Applied Sciences, PSOW, Environment and Climate Change Canada, Vancouver, BC, Canada

Key Points:

- Some heavy precipitation events can be attributed to the strong water vapor convergence induced by atmospheric rivers
- The column relative humidity and the primary condensation rate are two supplements to the standard weather analysis to help focus on the atmospheric river contribution to heavy precipitation
- The primary condensation rate can be used as a proxy for the large-scale precipitation rate
- An algorithm for diagnosing the primary condensation rate is proposed
- The primary condensation rate has the application potential in storm scaling and classification

Corresponding author: R. Mo, ruping.mo@canada.ca

Abstract

Landfalling atmospheric rivers (ARs) frequently trigger heavy and sometimes prolonged precipitation, especially in regions with significant orography. The presence and strength of ARs are often described using the integrated water vapor (IWV) and the integrated vapor transport (IVT). However, the associated precipitation is not directly correlated with these two variables. Instead the intensity of precipitation is mainly determined by the net convergence of moisture and the initial degree of saturation of the air column. In this study, a simple algorithm is proposed for estimating the heavy precipitation attributable to the IVT convergence. Bearing a strong resemblance to the Kuo-Anthes parameterization scheme for cumulus convection, the proposed algorithm calculates the large-scale primary condensation rate (PCR) as a proportion of the IVT convergence, with a reduction to account for the general moistening in the atmosphere. The amount of reduction is determined by the column relative humidity (CRH), which is defined as the ratio of IWV to its saturation counterpart. Our analysis indicates that the diagnosable PCR compares well to the forecast precipitation rate given by the numerical weather prediction model. It is also shown that the PCR in an air column with CRH < 0.50 is negligibly small. The usefulness of CRH and PCR as two complements to standard AR analysis is illustrated in some case studies. The potential application of PCR to storm classification is also explored.

1 Introduction

Water vapor forms the link between the Earth's surface and the atmosphere in the hydrologic cycle, and plays an important role in various atmospheric processes such as cloud formation, precipitation, energy transfer and conversion, radiation and climate change (Espy, 1841; Tyndall, 1863; McEwen, 1930; Houghton, 1951; Manabe & Wetherald, 1967; Jacob, 2001; Schneider et al., 2010). Because the moisture distribution is highly non-homogeneous both in space and time, water vapor transport is essential in shaping the global energy and water cycles. It has been demonstrated that a substantial fraction of the water vapor transport in the extratropical atmosphere can be attributed to a phenomenon called "atmospheric river" (AR), which is a long and narrow moist flow that may carry as much water as the Amazon River (Newell et al., 1992; Zhu & Newell, 1994, 1998). The AR development is typically associated with a low-level jet stream ahead of the cold front of an extratropical cyclone, and frequently leads to heavy precipitation at locations where the moist flow is forced upward by mountains or frontal systems (Ralph et al., 2004; Neiman et al., 2008; Lavers et al., 2011; Garreaud, 2013; Mahoney et al., 2016; Paltan et al., 2017; Blamey et al., 2018; Mo et al., 2019; Sharma & Déry, 2020; Ye et al., 2020; Xiong & Ren, 2021; American Meteorological Society, 2021).

The two commonly used fields to detect and define ARs are the vertically integrated water vapor (IWV) and the integrated vapor transport (IVT) (Newell et al., 1992; Zhu & Newell, 1998; Dettinger, 2004; Ralph et al., 2004; Lavers et al., 2012; Wick et al., 2013; Guan & Waliser, 2015; Pan & Lu, 2019). The IWV is also known as precipitable water vapor. It can be calculated from a moisture profile alone, and its value indicates the total water vapor content in a vertical air column. The use of IWV as a proxy for AR detection was established by Ralph et al. (2004) based upon its close correlation with IVT over the extratropical North Pacific. When both wind and moisture profiles are available, it is more appropriate to analyze ARs based on the IVT distribution. Recently, Ralph et al. (2019) introduced a scale for characterizing the strength and potential impacts of ARs based on the IVT intensity and the event duration. This 5-category scale has been widely used to communicate the benefits and hazards associated with ARs (Cruickshank, 2019; Zhang et al., 2019; Hatchett et al., 2020; Zhao, 2020).

The major impact of an AR is to produce large amounts and often high intensity of precipitation. However, neither the IWV nor the IVT can quantify the precipitation

intensity. Precipitation received at a location is mainly controlled by three factors: 1) the amount of available water vapor in the air; 2) the degree of air saturation represented by this vapor; 3) the presence of dynamic mechanisms that provide not only a continuous supply of moisture through transport, but also the cooling necessary to produce condensation and precipitation (Tuller, 1971, 1973). In a motionless atmosphere, the IWV value could be used to represent the potential maximum amount of precipitation if all the vapor above the Earth's surface were condensed and precipitated out. However, depending on the degree of saturation of the air column, the actual amount of condensation often accounts for only a small fraction of the IWV. The saturation level is determined by the vapor content in the air and the temperature profile. In reality, the amount of water vapor in an air column constantly changes due to moisture transport. Since the IWV does not account for additional water vapor advected into the column, it cannot estimate the actual precipitation amount (Tuller, 1973; Stull, 2017).

The IVT is a measure of overall strength of horizontal moisture flux. It is reasonable to expect that stronger IVT could bring more water vapor to an area and thereby lead to heavier precipitation. However, the IVT value and the quantity of precipitation could be poorly related, because precipitation is associated with net convergence rather than with moisture transfer (Benton & Estoque, 1954). Furthermore, the converged water vapor will be shared between condensation and a general moistening of the atmosphere, and the fraction of condensation depends on the degree of air column saturation (Kuo, 1974; Anthes, 1977; Sundqvist, 1978).

The main purpose of this paper is twofold: (i) to promote the use of the column relative humidity (CRH) as an appropriate measure of air column saturation (Bretherton et al., 2004); and (ii) to propose an algorithm to diagnose the primary condensation rate (PCR) attributed to the horizontal moisture convergence, which can be used to estimate the AR contribution to heavy precipitation. To quantify the concept of converged water vapor shared between condensation and air moistening (Sundqvist, 1978), the PCR is defined as a function of the CRH and the net convergence of horizontal moisture flux. It can be used as a proxy for the large-scale precipitation rate when condensed-water storage is neglected. Both CRH and PCR are diagnosable variables that can complement AR analysis.

The rest of the paper is organized as follows. Section 2 describes the data used in this study and the AR identification methods. Section 3 reviews the balance requirements for water in the atmosphere and gives the definitions of PCR and CRH. Some case studies are provided in Section 4 to illustrate how to make use of PCR and CRH in AR analysis, and how to determine the optimal parameters for the proposed PCR algorithm. The potential application of PCR to storm scaling is explored in Section 5. Further discussion and conclusions are given in Section 6.

2 Data Description and Atmospheric River Identifications

2.1 Data Sources

The model data used in this study are mainly extracted from the analyses and predictions of the operational Global Deterministic Prediction System (GDPS) of Environment and Climate Change Canada (ECCC). This numerical weather prediction (NWP) model uses a Yin-Yang grid with an approximate horizontal spacing of 15 km and an 84-level terrain-following, staggered log-hydrostatic-pressure vertical coordinate system (McTaggart-Cowan et al., 2019). It is currently run twice daily starting at 0000 and 1200 UTC, respectively. This model uses the modified Sundqvist scheme for grid-scale condensation parameterization, which assumes that the precipitating hydrometeors fall instantaneously to the ground. It uses a legacy grid-scale cloud scheme (Sundqvist et al., 1989) to pre-

dict large-scale clouds. In addition, three different parameterization schemes are employed to handle deep, shallow, and elevated convection.

Other data include a China weather radar mosaic obtain from China Meteorological Administration (`http://en.weather.com.cn/radar/`), a Prince George radar image from the Canadian Historical Weather Radar Archive (`https://climate.weather.gc.ca/radar/index_e.html`), and a USA radar mosaic from the National Centers for Environmental Information (`https://www.ncdc.noaa.gov/data-access/radar-data`). Hourly precipitation data in Canada are obtained from the ECCC data archive, and those in the USA are obtained from the Iowa Environmental Mesonet (`https://mesonet.agron.iastate.edu/archive/`).

2.2 Methods of AR Identification

The two most common fields used to identify ARs are IWV and IVT, which can be defined in a pressure (p) coordinate system as follows

$$\text{IWV} = W = \frac{1}{g}\int_{p_\text{t}}^{p_\text{b}} q\mathrm{d}p, \quad \text{IVT} = |\mathbf{Q}|, \quad \text{with } \mathbf{Q} = \frac{1}{g}\int_{p_\text{t}}^{p_\text{b}} q\mathbf{V}_\text{h}\mathrm{d}p, \tag{1}$$

where g is the acceleration due to gravity, q is the specific humidity, $\mathbf{V}_\text{h}$ is the horizontal wind vector, and p_b and p_t are the pressures at the bottom and the top of the air column, respectively. The vector $\mathbf{Q}$ is called the integrated water vapor flux (IWVF). The IVT is defined as the magnitude of IWVF.

Water can also be stored in the atmosphere in condensed (liquid and/or solid) phase. Therefore, the vertically integrated condensed water (W_c) and the integrated condensed water flux ($\mathbf{Q}_\text{c}$) can be similarly expressed by

$$W_\text{c} = \frac{1}{g}\int_{p_\text{t}}^{p_\text{b}} q_\text{c}\mathrm{d}p, \quad \mathbf{Q}_\text{c} = \frac{1}{g}\int_{p_\text{t}}^{p_\text{b}} q_\text{c}\mathbf{V}_\text{h}\mathrm{d}p, \tag{2}$$

where q_c is the specific amount of water in the condensed phase. In the atmosphere, the storage of water in the vapor phase is much larger than in the condensed phase (Peixoto, 1973). Therefore, it can be expected that $W \gg W_\text{c}$ and $|\mathbf{Q}| \gg |\mathbf{Q}_\text{c}|$.

Ralph et al. (2004) proposed a simple method for the AR identification based on the IWV distribution: an AR is an elongated moisture plume with core IWV values exceeding 20 kg m^{-2} for $\geq$ 2000 km in the along-plume direction and $\leq$ 1000 km in the cross-plume direction. ARs can also be identified based on the IVT distribution, such as an elongated area with a minimum IVT threshold of 250 (or 500) kg m^{-1}s^{-1}, a length $\geq$ 2000 (or 1500) km, and a length-to-width ratio $>$ 2 (e.g., Rutz et al., 2014; Guan & Waliser, 2015; Mahoney et al., 2016).

In theory, the vertical integration should be carried out from the Earth's surface to the top of the atmosphere ($p_\text{t} = 0$). However, since q decreases rapidly with height, integration up to the 300-hPa level usually suffices for practical applications (Zhu & Newell, 1998; Lavers et al., 2012). As an example, Fig. 1 plots the radiosonde profiles at Prince George in western Canada, valid at 0000 UTC 15 August 2020. The air temperature (T) and dewpoint (T_d) profiles in Fig. 1a indicate that the air column in the troposphere (below the 200-hPa level) was quite moist, especially in the lower levels between 600 and 850 hPa where $T - T_d \leq 2$°C. In Fig. 1b, both the specific humidity q and the saturation specific humidity q_s are very close to zero above the 300-hPa level; the formulas for calculating q and q_s are given in Appendix A.

The saturation IWV (W_s) in Fig. 1b and the saturation IVT ($|\mathbf{Q}_\text{s}|$) in Fig. 1c are obtained by replacing q in Eq. (1) with q_s, and they are given as functions of p_t that varies

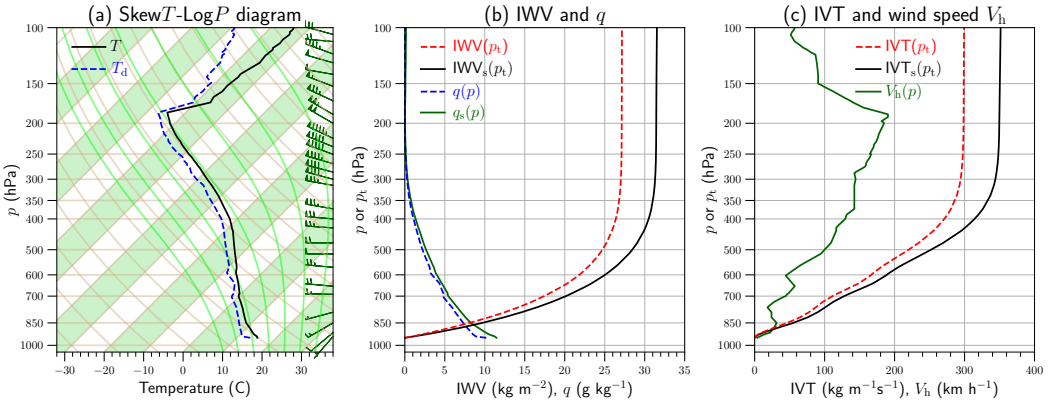

Figure 1. Upper-air analysis based on a sounding taken at Prince George, British Columbia, Canada (CZXS: 53.90°N, 122.79°W), valid at 0000 UTC, 15 August 2020. (a) The profiles of temperature (T), dewpoint (T_d), and wind vectors in the Skew$T$-Log$P$ diagram with a 45° rotation of isotherms relative to horizontal. (b) The profiles of specific humidity (q), saturation specific humidity (q_s), integrated water vapor (IWV), and integrated saturation water vapor (IWV$_s$). (c) The profiles of wind speed (V_h), integrated vapor transport (IVT) and its saturation counterpart (IVT$_s$). Note that q, q_s, and V_h vary with the pressure (p), while IWV, IWV$_s$, IVT, and IVT$_s$ vary with the integration limit p_t.

from p_b (947 hPa) to 100 hPa, i.e.,

$$\mathrm{IWV_s}(p_t) = W_s = \frac{1}{g}\int_{p_t}^{p_b} q_s \mathrm{d}p, \quad \mathrm{IVT_s}(p_t) = \frac{1}{g}\int_{p_t}^{p_b} q_s |\mathbf{V}_h| \mathrm{d}p. \tag{3}$$

Figure 1 shows that changing p_t from 300 hPa to 100 hPa has a negligibly small contribution to IWV or IVT, even with the assumption of a fully saturated layer (i.e., further increase in W_s or $|\mathbf{Q}_s|$ as p_t becomes less than 300 hPa is also negligible). Therefore, for most operational applications, it is acceptable to set $p_t = 300$ hPa in Eqs. (1) and (3). As a compromise between computational efficiency and accuracy in high-elevation areas (such as the Tibetan Plateau), we use $p_t = 200$ hPa in this study.

3 Water Balance Requirements in the Atmosphere

Since water cannot be created nor destroyed in the atmosphere, its local change can only occur through the addition or subtraction in any of its three possible phases (vapor, liquid, and solid), as described by the following balance equation (Peixoto, 1973):

$$\frac{\mathrm{d}(q+q_c)}{\mathrm{d}t} = \left[\frac{\partial q}{\partial t} + \nabla\cdot(q\mathbf{V}_h) + \frac{\partial(q\omega)}{\partial p}\right] + \left[\frac{\partial q_c}{\partial t} + \nabla\cdot(q_c\mathbf{V}_h) + \frac{\partial(q_c\omega_c)}{\partial p}\right] = 0, \tag{4}$$

where $\nabla\cdot$ is the two-dimensional horizontal divergence operator, $\omega = \mathrm{d}p/\mathrm{d}t$ is the vertical velocity in the p coordinate system, ω_c is the averaged vertical velocity of the condensed water (liquid droplets or solid ice particles) relative to air.

For the total water balance, precipitation and evaporation at the Earth's surface must be considered. If the effects of climate change are ignored, over a long period of time the total water content in the atmosphere should not suffer any appreciable change, leaving the total global precipitation to be balanced by the corresponding evaporation in the hydrological cycle. Such a balance does not necessarily apply to a regional domain and over a synoptic timescale. For a persistent heavy precipitation event, the horizontal transport of water vapor becomes a necessary condition.

3.1 Water Balance Within an Air Column and Precipitation

Vertically integrating Eq. (4) from the bottom to the top of the atmosphere gives an equation that links precipitation and evaporation measured at the Earth's surface (boundary conditions) with the total water balance within an air column,

$$P = E - \frac{1}{\rho_{\mathrm{w}}}\left(\frac{\partial W}{\partial t} + \nabla\cdot\mathbf{Q}\right) - \frac{1}{\rho_{\mathrm{w}}}\left(\frac{\partial W_{\mathrm{c}}}{\partial t} + \nabla\cdot\mathbf{Q}_{\mathrm{c}}\right). \tag{5}$$

In the above equation, P and E are the rates of downward precipitation and upward evaporation, and $\rho_{\mathrm{w}} = 1000$ kg m^{-3} is the liquid water density. The quantities $\partial W/\partial t$ and $\partial W_{\mathrm{c}}/\partial t$ represent the rates of change in vapor phase and in condensed phase of water storage within the air column, respectively. The terms $\nabla\cdot\mathbf{Q}$ and $\nabla\cdot\mathbf{Q}_{\mathrm{c}}$ are the divergences of water vapor flux and condensed water flux, respectively. The inclusion of ρ_{w} in this equation means that the unit for P and E can be conveniently chosen as m s^{-1}, mm h^{-1} or mm (24h)$^{-1}$.

The storage of water in the atmosphere in the vapor phase is much larger than that in the condensed phase, and the same applies to their local time rates of change, i.e., $\partial W/\partial t \gg \partial W_{\mathrm{c}}/\partial t$ (Peixoto, 1973). While the divergence of condensed water flux, $\nabla\cdot\mathbf{Q}_{\mathrm{c}}$, can at times be as important as the divergence of vapor flux, $\nabla\cdot\mathbf{Q}$ (Peixoto, 1973; Mo et al., 2019), its role in the precipitation process is often considered as secondary (Starr & Peixoto, 1958; Trenberth & Guillemot, 1998; Stohl & James, 2004; Cordeira et al., 2013; Mo & Lin, 2019). For a heavy precipitation event, the contribution from local evaporation is negligible, and the dominant factor is the net condensation rate (CR) represented by the second term on the right-hand side of Eq. (5),

$$\mathrm{CR} = -\frac{1}{\rho_{\mathrm{w}}}\left(\frac{\partial W}{\partial t} + \nabla\cdot\mathbf{Q}\right) = -\frac{1}{\rho_{\mathrm{w}}}\left[\left(\frac{\partial W}{\partial t}\right)_{\mathrm{p}} + \nabla\cdot\mathbf{Q} + \left(\frac{\partial W}{\partial t}\right)_{\mathrm{s}}\right] = \mathrm{PCR} + \mathrm{SCR}. \tag{6}$$

In the above equation, CR is further partitioned into a primary condensation rate, $\mathrm{PCR} = -\rho_{\mathrm{w}}^{-1}[(\partial W/\partial t)_{\mathrm{p}} + \nabla\cdot\mathbf{Q}]$, which is attributed solely to the convergence of IWVF that results in general moistening and condensation, and a secondary condensation rate (SCR) due to other factors (e.g., radiative cooling and/or cold advection).

3.2 An Algorithm for Diagnosing the PCR Based on the CRH

The PCR in Eq. (6) can be parameterized into a non-negative, diagnosable variable,

$$\mathrm{PCR} = \begin{cases} -a\rho_{\mathrm{w}}^{-1}\nabla\cdot\mathbf{Q}, & \text{if } \nabla\cdot\mathbf{Q} < 0, \\ 0, & \text{if } \nabla\cdot\mathbf{Q} \geq 0, \end{cases} \tag{7}$$

with $0 \leq a \leq 1$. It is assumed that a fraction a of the total converged water vapor is condensed, while the remaining fraction $(1-a)$ is stored in the air to increase the humidity (Kuo, 1974). For an AR-induced heavy precipitation event, it may be safely assumed that PCR $\gg$ SCR and so the PCR should be the dominant factor on the right-hand side of Eq. (5), i.e., $P \approx$ PCR (Mo et al., 2019; Mo & Lin, 2019).

For a fully saturated air column, any moisture convergence should be balanced by condensation, i.e., $a = 1$. The degree of the air column saturation can be measured by the CRH defined by (Bretherton et al., 2004)

$$\mathrm{CRH} = \Re = W/W_{\mathrm{s}}. \tag{8}$$

As an example, the CRH for the sounding shown in Fig. 1 is 0.86. In this study, we assume that a in Eq. (7) is a function of the CRH in the following form (*cf.* Anthes, 1977)

$$a = \begin{cases} \left[(\Re - \Re_{\mathrm{c}})/(1-\Re_{\mathrm{c}})\right]^n, & \text{if } \Re > \Re_{\mathrm{c}}, \\ 0, & \text{if } \Re \leq \Re_{\mathrm{c}}, \end{cases} \tag{9}$$

where $\Re_c$ and n are parameters that may be empirically adjusted. Their optimal values will be determined in Section 4. Note that Anthes (1977) used a similar formula in a cumulus parameterization scheme, i.e., $a = 1 - [(1 - \langle \mathrm{RH} \rangle)/(1 - \mathrm{RH_c})]^n$ if $\langle \mathrm{RH} \rangle \geq \mathrm{RH_c}$, otherwise $a = 0$. Here $\langle \mathrm{RH} \rangle$ is the mean relative humidity in the air column. For AR analyses dealing with large-scale precipitation, CRH is better than $\langle \mathrm{RH} \rangle$ as a column saturation index, because it gives less weight to the upper atmosphere where the specific humidity is much lower than it is in the lower atmosphere (Fig. 1b). We have also tested Anthes' formula with $\langle \mathrm{RH} \rangle$ replaced by $\Re$. Its performance is not better than that of Eq. (9).

4 Case Studies and Parameter Optimization

In this section, we perform some case studies to demonstrate the usefulness of PCR and CRH as two supplements to standard AR analysis. Our case studies focus on three AR events identified over East Asia and North America in mid-August 2020. We also make use of a full year of NWP model data to determine the optimal values of n and $\Re_c$ for the PCR algorithm in Eq. (9).

4.1 IVT, IWV and Synoptic Weather Analysis

Figure 2 gives a snapshot of AR conditions at 0000 UTC 15 August 2020. The global IVT/IWVF distribution (Fig. 2a) shows multiple AR-like structures around the world. There were at least four ARs in the Southern Hemisphere: one across the South American continent and the other three over the Indian Ocean. There was also an AR-like structure over the South Pacific Ocean flowing towards southern Chile. In the Northern Hemisphere, the moist monsoonal flow across the Arabian Sea, southern India, and the Bay of Bengal may be considered as a giant AR. As this system moved across the Indochinese Peninsula, it turned north and penetrated through the mainland of China, the Korean Peninsula, and Japan (Fig. 2b). Over North America, there was a well-defined AR over the Northeast Pacific Ocean that just made landfall on the west coast of Canada, and a cyclone in northern Canada had spun up a continental AR that can be traced into the upper midwestern United States (Fig. 2c). Note that the IWVF vectors in Fig. 2a are normalized for easier visualization.

The major driving forces behind the AR across East Asia (Fig. 2b) include 1) the subtropical high pressure system in the northwestern Pacific Ocean that forced the monsoonal flow to change direction and penetrate through the mainland of China (e.g., Chen et al., 2020); 2) the high plateaus in western China that often act as a orographic barrier which intercepts and guides the tropical moist flow northwards through China (Lu, 1947); 3) a cold front associated with an occluded cyclone centered at (50°N, 128°E), which dragged the moist flow further into the extratropical North Pacific. This AR system started to form over eastern China on 12 August and lasted for more than four days with severe hydrometeorological impacts. It produced numerous heavy precipitation events across areas from southwestern to northern China, and the rain-induced floods for the following few days devastated the Yangtze Basin and caused the worst flood-related damages ever seen in Chongqing, a megacity in Southwest China (Huang, 2020; Shih, 2020; Tan & Li, 2020).

The AR over the Northeast Pacific Ocean (Fig. 2c) made landfall on the west coast of Canada around 0600 UTC 14 August 2020. It was jointly driven by a mobile cyclone over the Gulf of Alaska and a quasi-stationary anticyclone to the south. It triggered some heavy rainfall over the north and central coast of British Columbia (BC) and caused some landslides near the city of Prince Rupert (Millar, 2020). The AR system also spread moderate precipitation into the central interior and northern BC.

Also noticeable in Fig. 2c is a continental AR across North America, driven by an occluded cyclone over the Northwest Territories in Canada and a rapidly developing cy-

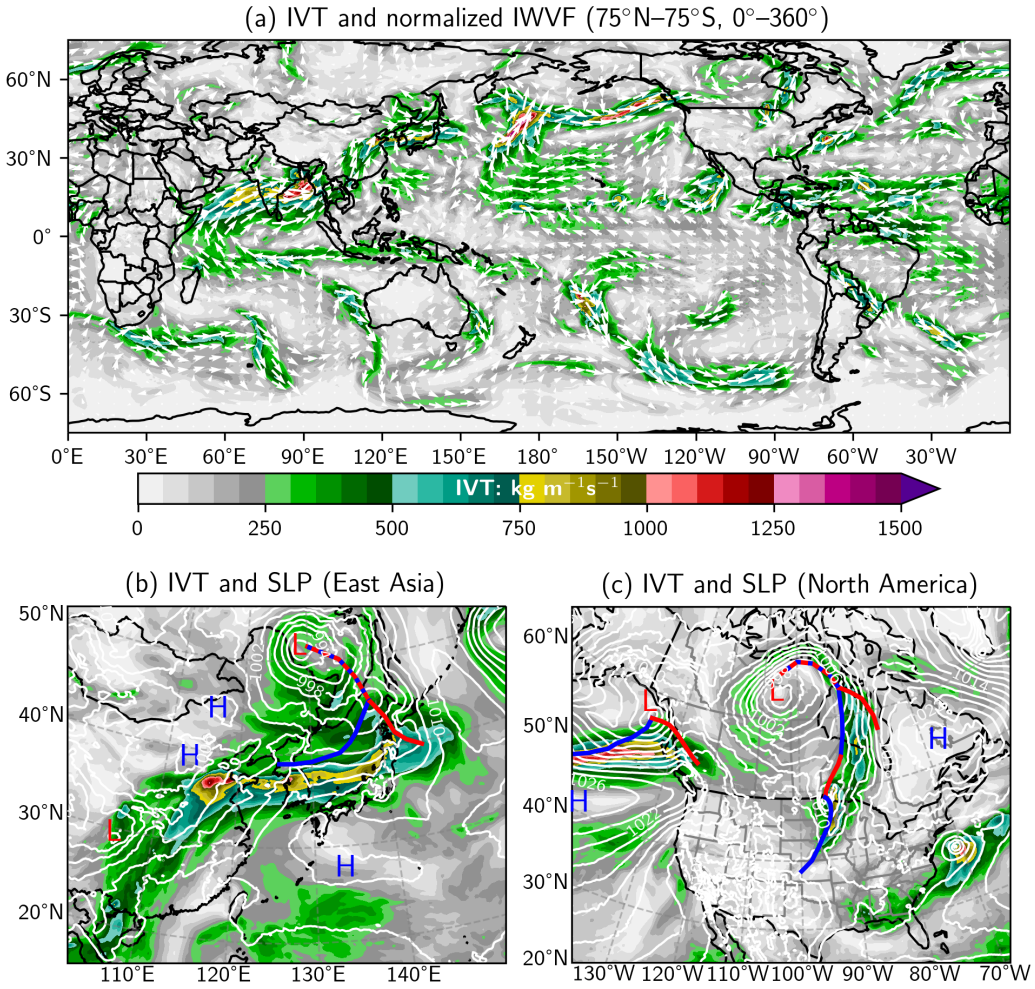

Figure 2. Atmospheric river conditions based on the GDPS analysis (0-hour forecast fields), valid at 0000 UTC 15 August 2020. (a) Global distributions of IVT (color-filled) and normalized IWVF vectors, $\hat{\mathbf{Q}} = \mathbf{Q}/(|\mathbf{Q}| + 250\,\mathrm{kg\,m^{-1}s^{-1}})$. (b) IVT (color-filled), sea level pressure (SLP, line contours with intervals of 2 hPa), and frontal analysis for an East Asian domain. (c) The sames as (b), except for a North American domain. Cold and warm fronts are represented by blue and red solid lines, respectively, and occluded fronts are marked by red-blue dashed lines. Centers of low and high pressure are marked by L and H, respectively.

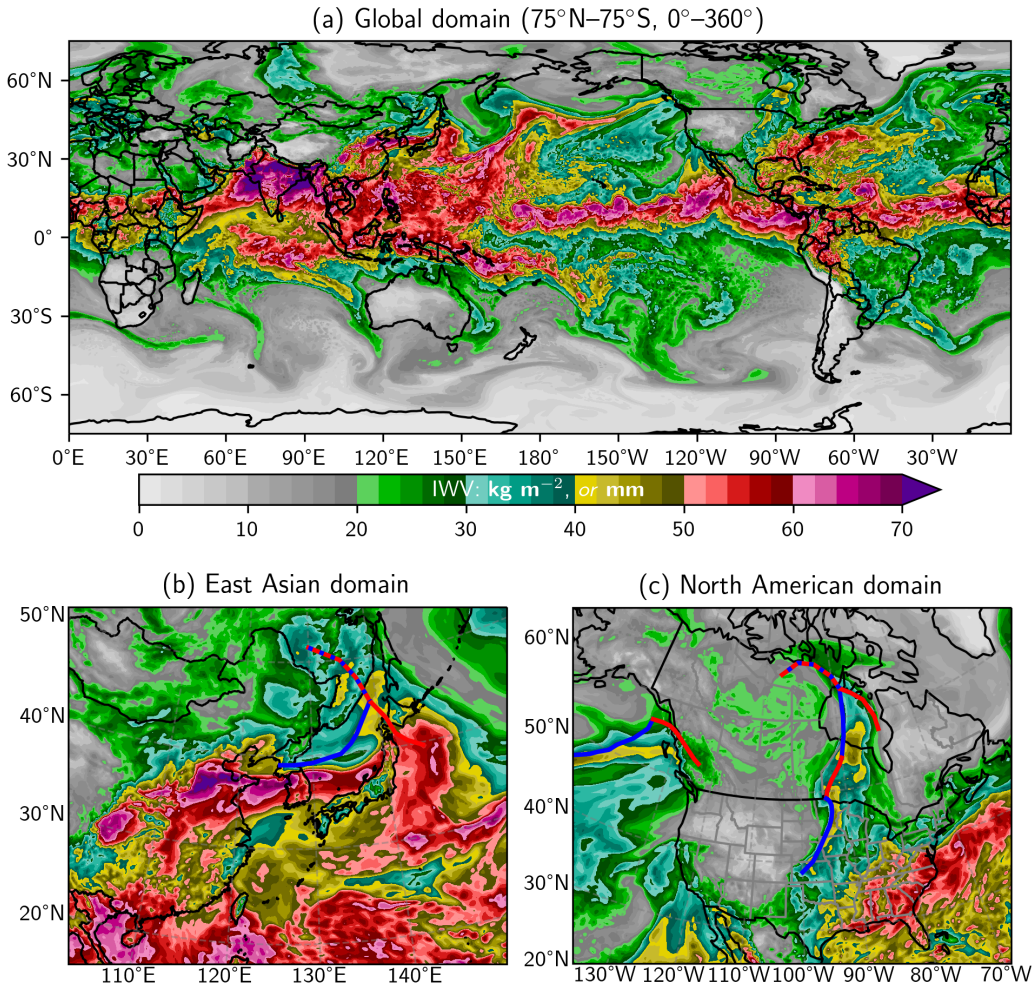

Figure 3. Integrated water vapor distribution and frontal systems based on the GDPS analysis, valid at 0000 UTC 15 August 2020.

clone near the USA-Canada border. It is called a *continental* AR because the apparent source of the moisture feeding into this system is land-based (*cf.* Liu et al., 2016; Li et al., 2017; Mo & Lin, 2019). Severe thunderstorms associated with this system produced damaging winds, flash flooding, funnel clouds and tornadoes through Minnesota and Wisconsin (National Weather Service, 2020). Severe thunderstorms were also observed in southeastern Manitoba and northwestern Ontario as the AR moved across these areas, as shown later in this section.

Figure 3 shows the IWV distribution valid at 0000 UTC 15 August 2020. In the Southern Hemisphere (winter season), the three IWV filamentary structures over the Indian Ocean correspond well to the ARs identified with the IVT field. The subtropical AR across the South American continent only has a well-defined southern boundary in the IWV field. In the Northern Hemisphere (summer season), the IWV values are very high over tropical and subtropical areas, and because of this it is hard to identify the filamentary structure of some ARs. In particular, the AR over East Asia is poorly defined in terms of IWV (Fig. 3b).

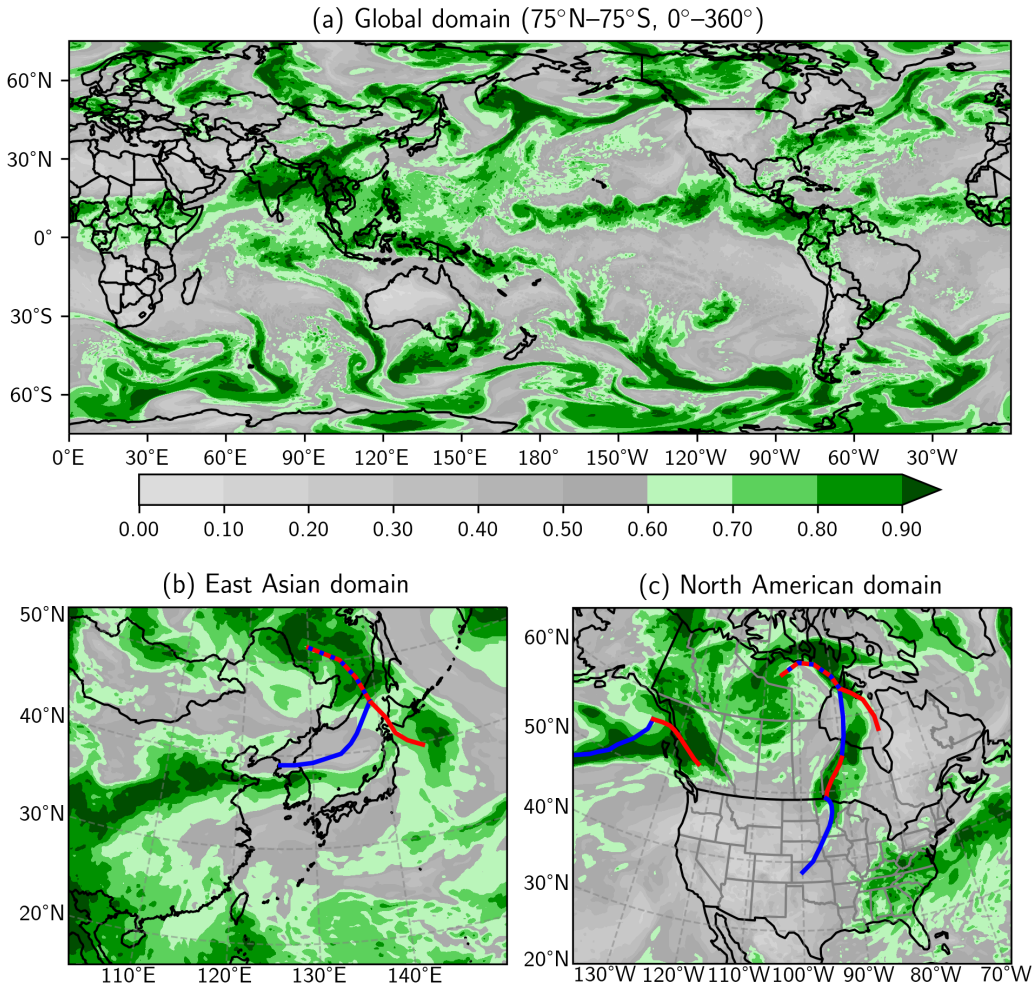

Figure 4. The CRH distribution and frontal systems based on the GDPS analysis, valid at 0000 UTC 15 August 2020.

4.2 The Distributions of CRH and Forecast Precipitation Rate

The corresponding CRH distribution is shown in Fig. 4. It can be taken as a useful supplement to standard AR maps to help focus attention on the moist areas where precipitation efficiency is high. Generally, the ARs are much easier to identify here than in Fig. 3. Comparing Fig. 4 with Fig. 2 highlights that bands of large CRH are not always co-located with bands of strong IVT. For example, the CRH-AR over China (Fig. 4b) is shifted further north of the IVT-AR (Fig. 2b).

The 24h lead time forecast precipitation rate (FPR) valid at 0000 UTC 15 August 2020 is plotted in Fig. 5. This is based on the operational prediction of the ECCC GDPS initialized at 0000 UTC 14 August. A narrow band of heavy precipitation can be seen over China in Fig. 5b, which is co-located with the band of maximum CHR in Fig. 4b and slightly shifted to the north of the maximum IVT in Fig. 2b. Over North America, heavy precipitation was also forecast on the north and central coast of BC, where the onshore moist flow of the Pacific AR was intercepted by the Coast Mountains. The warm front also spread some rainfall into the BC interior. There was also a narrow band of heavy

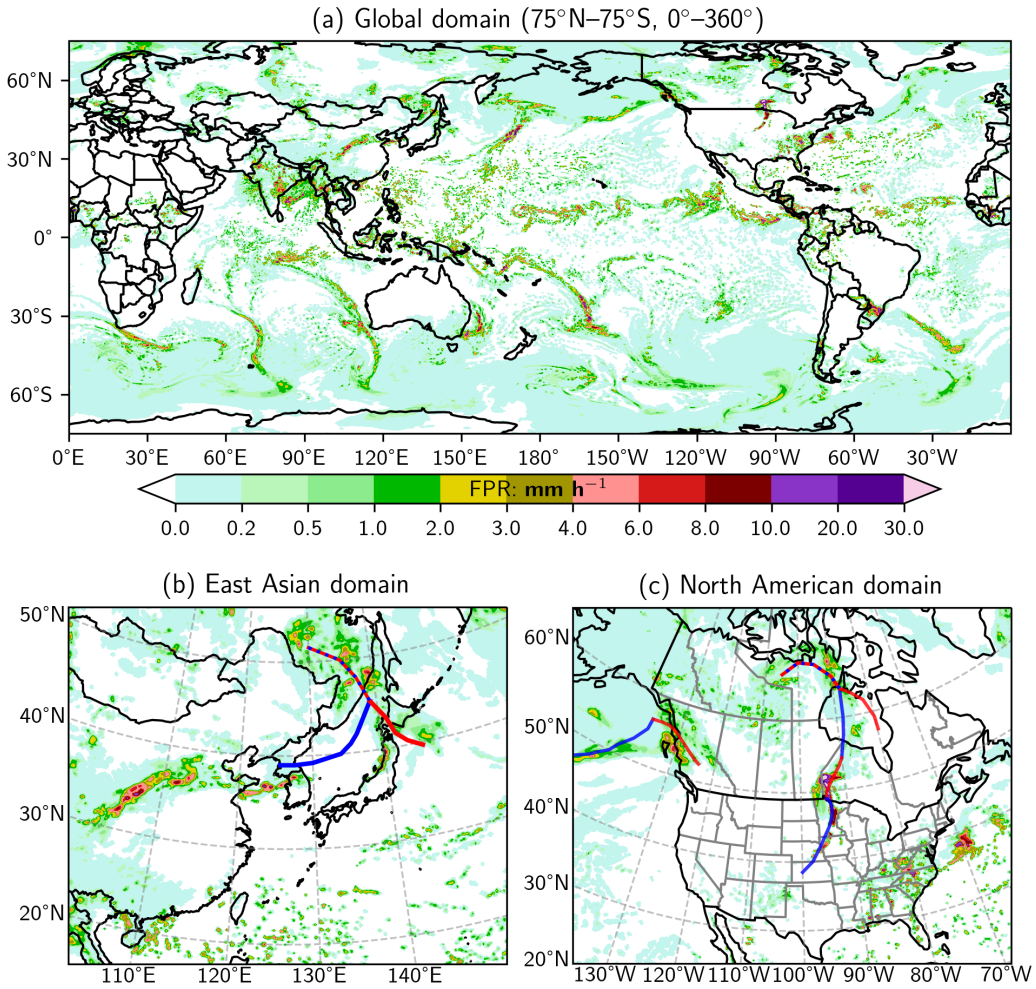

Figure 5. The forecast precipitation rate (FPR) distribution with frontal analysis valid at 0000 UTC 15 August 2020. This is the 24h lead time prediction by the operational GDPS run initialized at 0000 UTC 14 August 2020.

precipitation associated with the continental AR across the upper midwestern United States and northwestern Ontario in Canada.

4.3 Optimal Parameters for the PCR algorithm

The FPR in Fig. 5 was derived from the GDPS operational forecast output. It was calculated based on a complicated scheme in the NWP model to simulate various thermodynamic processes, including deep, shallow, and elevated convection as well as large-scale clouds and precipitation (McTaggart-Cowan et al., 2019). To estimate the contribution from horizontal water vapor transport, we can calculate the PCR from Eq. (7) based on the forecast IVT and CRH fields and compare it with the FPR in Fig. 5. As a first step, we can take the FPR as a reference to find the optimal values of n and $\Re_c$ in Eq. (9). Figure 6 shows the global-average root mean-squared error (RMSE) between the FPR and the corresponding 24h forecast PCR with n varying from 0 to 2.5 and $\Re_c$ from 0 to 1, valid at 0000 UTC 15 August 2020. The optimal parameters for Eq. (9) estimated from this case are $n = 1.17$ and $\Re_c = 0.63$.

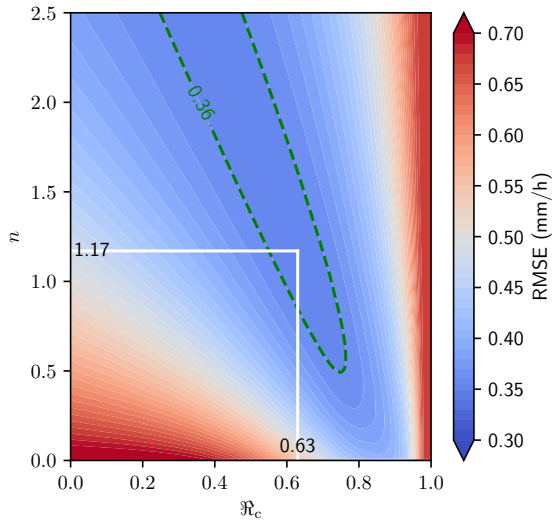

Figure 6. Global-average root mean-squared error (RMSE) between the FPR and the PCR based on the GDPS 24h lead time prediction, valid at 0000 UTC 15 August 2020. The minimum RMSE is located at $n = 1.17$ and $\Re_c = 0.63$.

There could be large case-to-case variability in this kind of parameter estimation. To address this concern, we use a full year of GDPS 24h forecast output (from 1 January to 31 December 2020) to create a 732-member ensemble and calculate the optimal parameters for each model run. The results are shown in Fig. 7. The ensemble-mean optimal parameters for Eq. (9) are $n = 1.25 = 5/4$ and $\Re_c = 0.60$. There is indeed some case-to-case variability due to either random effects or seasonal variation of atmospheric conditions. Nevertheless, the ensemble points are spread around a linear regression line relating the optimal $\Re_c$ to the specified n as follows

$$\Re_c = 0.826 - 0.177n. \tag{10}$$

For $n = 1$, this regression equation gives $\Re_c = 0.65$ as the optimal value. In a preliminary study with a different ensemble dataset (from 1 November 2019 to 31 October 2020), Mo (2020) let $n = 1$ and found that the best value for $\Re_c$ was 0.66. Figure 8 shows the coefficient a as a function of $\Re$ in Eq. (9) for some selected n with the corresponding $\Re_c$ based on the regression relation (10). The table embedded in Fig. 8 also lists the ensemble-mean RMSE (Fig. 7) for each pair of n and $\Re_c$. It shows that, for n ranging from 1.10 to 1.70, the algorithm achieves practically the same level of accuracy. Note that the coefficient a for each of the 13 selected pairs of parameters in Fig. 8 is either equal or very close to zero for $\Re < 0.50$, suggesting that the contribution of water vapor convergence to precipitation in the areas with $\Re < 0.50$ is generally negligible. Figure 8 also shows that especially for values of $\Re > 0.7$, given a specific $\Re$ the value of a does not change appreciably for any $\Re_c$ and n combination found along the minimum RMSE regression line. This suggests that for a given CRH a fairly specific amount of water vapor convergence must go to moistening the column rather than to precipitation. Unless stated otherwise, in this study we choose the ensemble-mean optimal parameters, $n = 5/4$ and $\Re_c = 0.60$, for Eq. (9).

4.4 Comparisons of PCR with FPR and Observations

Figure 9 shows the PCR distributions in East Asia and North America, using two different $(\Re_c, n)$ pairs and derived from the 24h lead time forecast fields valid at 0000

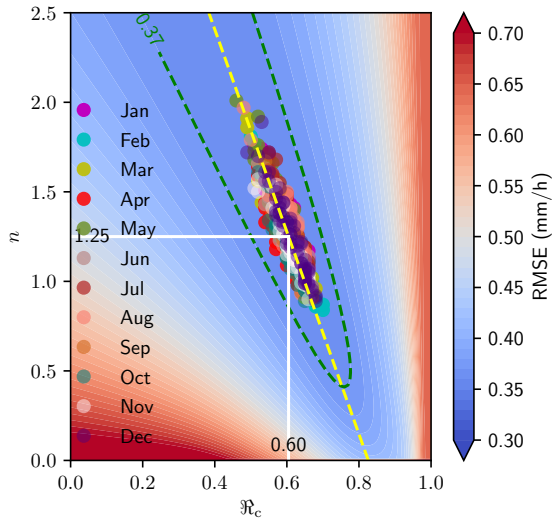

Figure 7. A full-year ensemble of global-average RMSE between the FPR and the PCR based on the GDPS 24h lead time prediction. The 732 ensemble members are from the GDPS twice-daily runs, initialized at 0000 and 1200 UTC respectively, from 1 January to 31 December 2020. The color-filled contour pattern represents the ensemble-mean global-average RMSE and the colored dots indicate the minimum RMSE of each ensemble member. The ensemble-mean minimum RMSE is located at $n = 1.25$ and $\Re_c = 0.60$. A regression equation obtained from the ensemble data is $\Re_c = 0.826 - 0.177n$, which is indicated by the yellow dashed line.

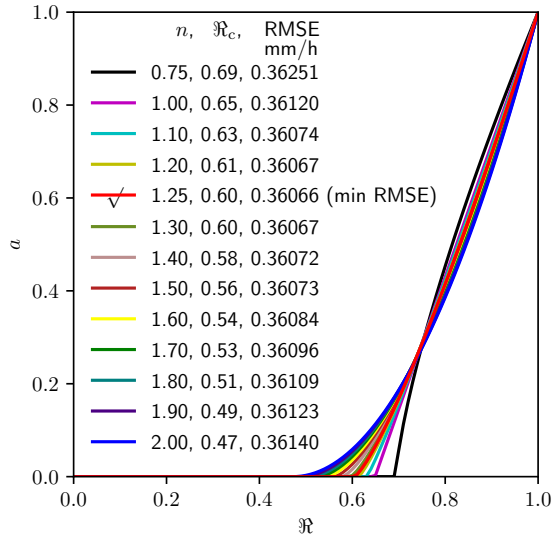

Figure 8. Variation of a defined in Eq. (9) as a function of $\Re$ for some selected parameters n and the optimal $\Re_c$ determined by the regression relation (10). The corresponding ensemble-mean RMSE (mm h^{-1}) in Fig. 7 is given in the embedded table.

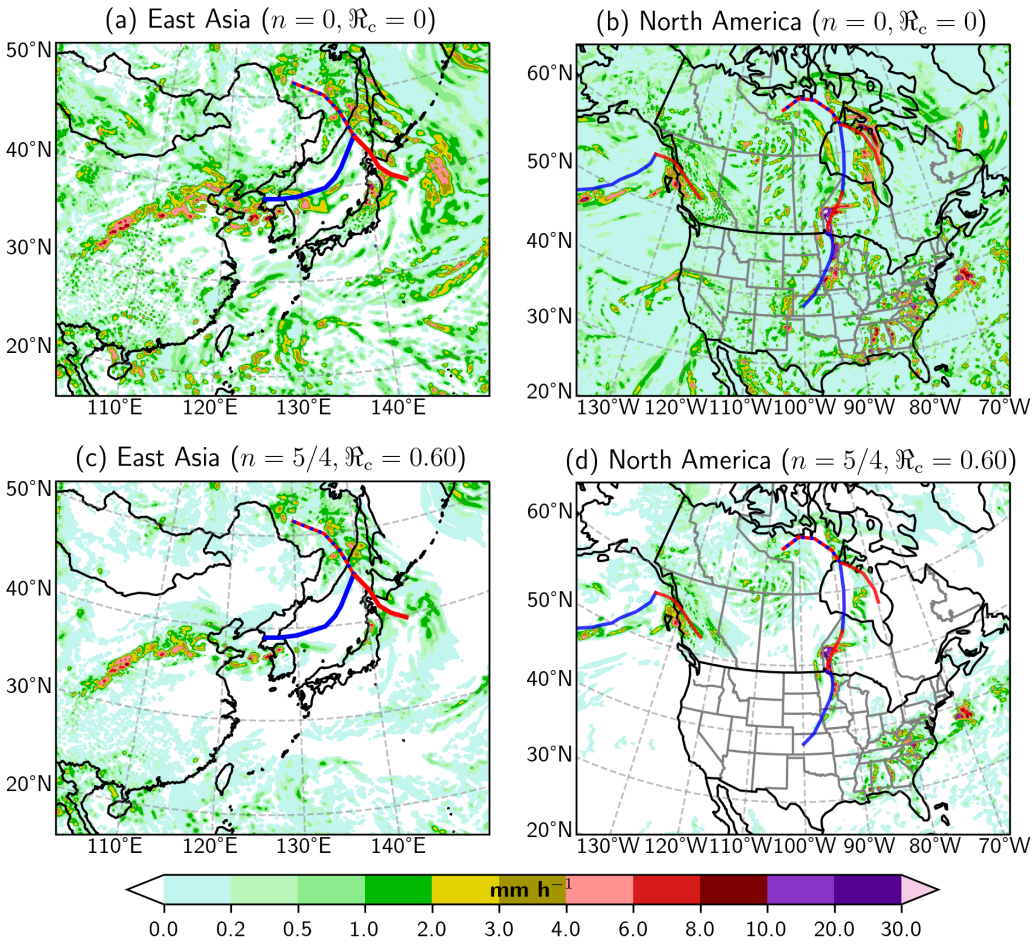

Figure 9. The PCR distributions for two sets of selected parameters: 1) $n = 0$, $\Re_c = 0$ ($a \equiv 1$), and 2) $n = 5/4$ and $\Re_c = 0.60$. The PCR is derived from the 24h lead time forecast fields valid at 0000 UTC 15 August 2020.

UTC 15 August 2020. The choice of $n = 0$ and $\Re_c = 0$ in (a) and (b), which corresponds to $a \equiv 1$, is for demonstration purposes. The corresponding PCR reflects its maximum potential contribution to precipitation from the horizontal water vapor convergence in a fully saturated atmosphere. In reality, a fraction of the converged vapor contributes to the general moistening ($\partial W/\partial t > 0$) in the unsaturated areas of the atmosphere. This contribution accounts for the differences between Figs. 9a and 9c (Figs. 9b and 9d). Note that, when comparing Fig. 9c with Fig. 9a, we can see some areas where PCR = 0 in Fig. 9c and PCR > 0 in Fig. 9a. This is because $\Re$ in these areas is lower than 0.60, so that $a = 0$ in Fig. 9c. The same applies to the comparison of Fig. 9d with Fig. 9d.

Comparison of Fig. 9c with Fig. 5b shows the band of heavy precipitation forecast over China is well captured in the PCR field, indicating that, despite a noticeable location shift between the rain band and the maximum IVT axis (Fig. 2b), the heavy precipitation can be attributed to the large-scale horizontal moisture convergence associated with the AR transport. Some differences in detailed structure of the FPR and the PCR along this band are understandable because the PCR is a diagnosed variable that is incapable of simulating sub-grid-scale convection. Comparing Fig. 9d with Fig. 5c also shows the strong similarity between the FPR and PCR patterns in the heavy precipi-

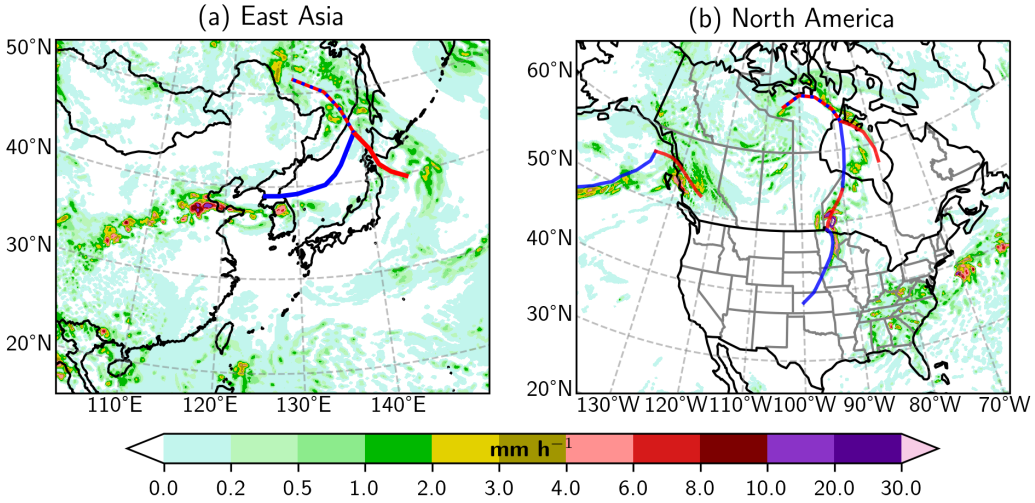

Figure 10. The PCR distribution derived from the GDPS analysis valid at 0000 UTC 15 August 2020.

tation areas over North America, particularly over the north coast of BC and northwestern Ontario in Canada. Note that the small differences between FPR and PCR in other areas could be attributed to the secondary condensation rate or other factors included in Eq. (5), such as cloud drift and evaporation.

It should be emphasized that the PCR is not designed to be an alternative to the FPR for operational forecast practice. Operational meteorologists need to analyze the FPR field for their quantitative precipitation forecast (QPF). PCR can help the forecasters better quantify the contribution from the horizontal water vapor transport (AR) to the QPFs. When the QPF tools are not available, such as in some post-storm case studies or storm classification schemes, the diagnosable PCR can serve as a proxy for precipitation rate in AR analysis. The following example illustrates the use of PCR for ad hoc model verification and precipitation diagnosis.

Figure 10 shows the PCR distributions in East Asia and North America based on the GDPS analysis (0-hour prediction) valid at 0000 UTC 15 August 2020. They can be used to verify the forecast distributions shown in Fig. 9. Because precipitation rate is not available in the GDPS analysis, Fig. 10 can also be used to verify the corresponding FPR distributions in Fig. 5. Comparing Fig. 10a with Fig. 9c or Fig. 5b shows the overall pattern of heavy rain over China being well predicted. The rain band in Fig. 10a is more disorganized than forecast, and some rainfall near the tail of the cold front was under-forecast in Fig. 5b and Fig. 9c. Note that the heavy rain band in Fig. 10a is consistent with the weather radar echo pattern shown in Fig. 11a.

The forecast quality in North America can be examined by comparing Fig. 10b (analysis) with Fig. 9d or Fig. 5c (forecast). Here the analyzed PCR in Fig. 10b (NWP initial condition) serves as a proxy for observed precipitation rate. It appears that the rainfall along the central and north coast of BC was slightly over-forecast and in the interior was under-forecast. The interior precipitation pattern in Fig. 10b can be compared with the echo pattern of the Prince George radar (CXPG: 53.61°N, 122.59°W) shown in Fig. 11b; there was no weather radar coverage for the rainy area on the coast. Hourly precipitation amounts observed at weather stations across BC are plotted in Fig. 12b. The heavy precipitation over the central coast of BC was confirmed by two stations, which reported hourly amounts from 8 to 10 mm. Over the BC north coast, the difference be-

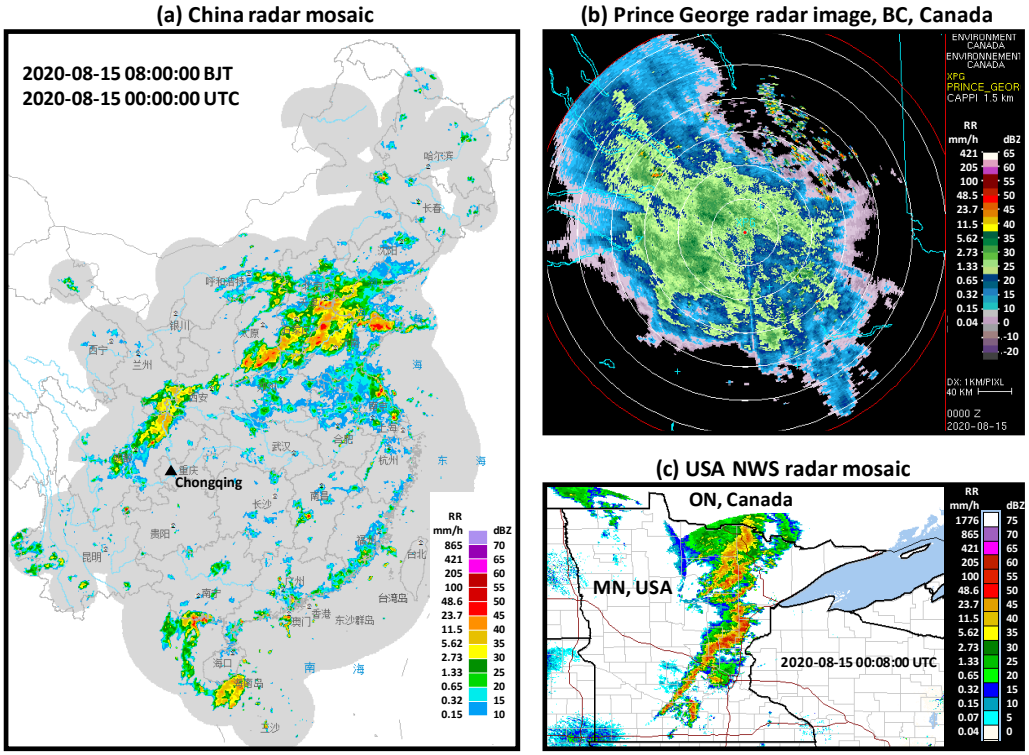

Figure 11. Weather radar images valid at around 0000 UTC 15 August. (a) Radar mosaic in China. (b) Echos on the 1.5-km CAPPI (Constant Altitude Plan Position Indicator) of the Prince George radar (CXPG: 53.61°N, 122.59°W); a further geo-reference for this radar can be seen in Fig. 12. (c) The USA National Weather Service radar mosaic in the upper midwestern United States. The rain rate (RR) is converted from the decibels of reflectivity factor, dBZ, using this Marshall-Palmer formula: $\mathrm{RR} = [10^{(\mathrm{dBZ}/10)}/200]^{5/8}$ (Marshall & Palmer, 1948).

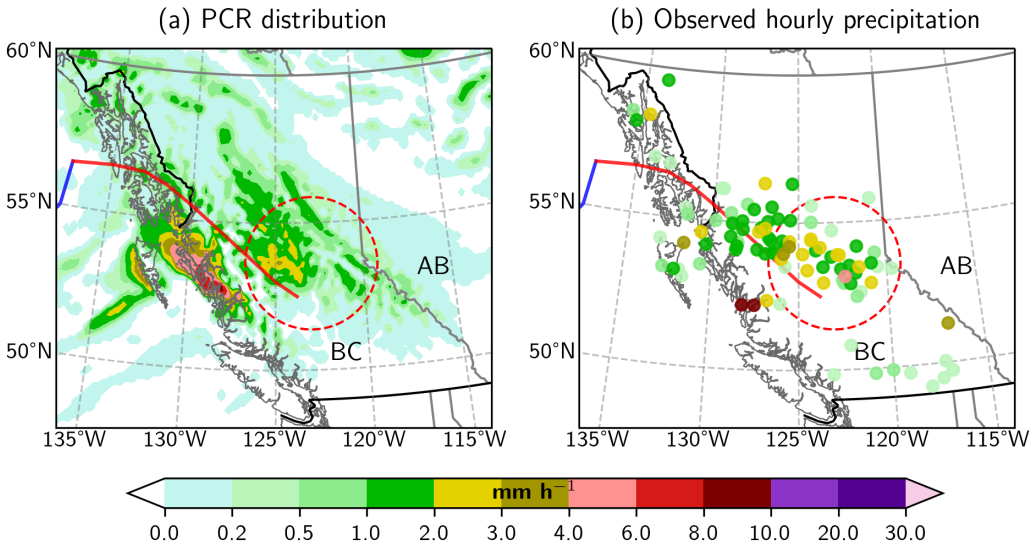

Figure 12. (a) The PCR distribution as in Fig. 10b, but in a smaller domain centered on British Columbia, Canada. (a) The maximum hourly precipitation amounts at weather stations valid at 0000 or 0100 UTC 15 August 2020. The red-dashed circle corresponds to the 250-km range of the Prince George radar in Fig. 11b.

tween the analyzed PCR and observed hourly rainfall amounts could be attributed to the spillover effect caused by the $\nabla \cdot \mathbf{Q}_c$ term in Eq. (5); see the relevant case studies on the BC south coast by Mo et al. (2019). Ahead of the warm front in the central interior of BC, the PCR pattern is close to the hourly observations in Fig. 12b.

The analyzed PCR distribution over the upper midwestern United States and near the Manitoba-Ontario border in Canada can be compared with the radar echoes in Fig. 11c and the observed hourly precipitation amounts in Fig. 13. The PCR pattern is quite consistent with the radar echoes and hourly observations. Ahead of the cold front in Minnesota, some observed amounts are higher than the corresponding PCR values, most likely due to strong convection. On the other hand, the bull's-eye structure in the PCR near the warm front was unconfirmed by observations in northwestern Ontario, where the density of weather stations was relatively low and radar data were unavailable because the two nearby Canadian weather radars (located at Woodlands, MB and Dryden, ON) were down for maintenance.

5 A Potential Application to the AR Classification

It was illustrated above that the PCR and CRH are useful supplements to routine AR analysis. A potential application of PCR to AR scaling is explored in this section.

Ralph et al. (2019) have recently introduced a scale for AR analysis. This five-category scale is based on the IVT intensity and duration thresholds over a location, assuming that the AR impacts are proportional to the AR strength. It can be used to characterize AR strength and potential impacts in a simple way that is both useful to scientists and conducive to communication with non-experts. In this scaling system, the AR impacts are implied, but not directly quantified. It is desirable and possible to add an impact component to this system based on the mean precipitation rate (MPR), which can be calculated from either the model FPR or the diagnosable PCR. Table 1 and Fig. 14

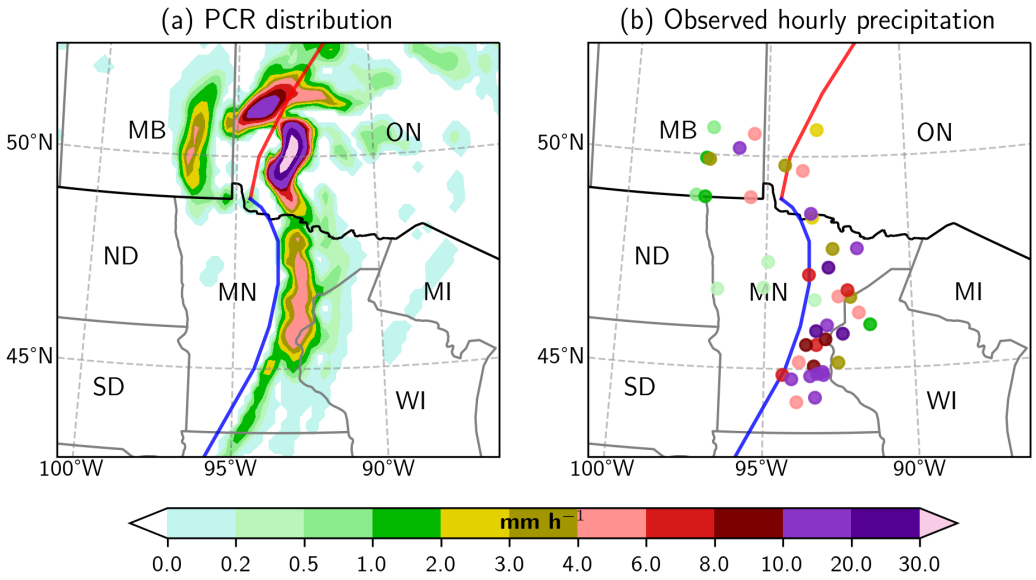

Figure 13. Same as Fig. 12, except for a domain in the upper midwestern United States and south-central Canada.

outline a possible combined scale given in the format of SxPy, where "Sx" stands for the strength scale based on the IVT method of Ralph et al. (2019) and "Py" represents the precipitation impact component. Thus, if an AR moves across a location with a duration of 40h and a maximum IVT of 800 kg m^{-1}s^{-1}, it is categorized as an S3 AR based on its strength. If the predicted or analyzed MPR over this 40h period is 120 mm (24h)$^{-1}$, it is classified as a P4 storm based on its precipitation impact.

Therefore, the combined scale for this AR at this location can be given as S3P4. It should be emphasized that, although two different scales are combined into one chart in Fig. 14, there is no implication of a one-to-one correspondence between the two scales. The S-scale is based on the maximum IVT on the left axis, and the P-scale is based on the MPR on the right axis. They are quasi-independent, given that the MPR is calculated from FPR or PCR over the AR duration determined by IVT threshold (IVT $\geq$ 250 kg m^{-1}s^{-1}).

Figure 15 shows an experimental application of the above-mentioned combined scale for the mid-August AR at selected locations in western Canada. It is based on the GDPS prediction initialized at 0000 UTC 13 August 2020. The color-coded dots on the zoomable map indicate the predicted strength scale (S-scale) for the corresponding weather stations. On the web-based application, clicking on a station will present the user with two time series of IVT and FPR; the IVT-based AR duration is color-filled based on the corresponding S-scale and P-scale. In this example, the MPR values calculated from the FPR and the PCR are indicated by the black dashed line and the red dotted line, respectively. The predicted strength and duration of this AR at Sandspit are similar to those at Prince Rupert, as illustrated in the IVT time series. However, the AR impacts on precipitation at these two stations are quite different; the stronger orographic forcing near Prince Rupert led to much heavier rainfall as suggested by the FPR time series. The MPR calculated from FPR (or PCR) at Sandspit over the 66h storm period is 7.3 (9.7) mm (24h)$^{-1}$, as compared to 56.0 (57.4) mm (24h)$^{-1}$ at Prince Rupert. Therefore, it would be appropriate to call this storm as an extreme AR with negligible impact

Table 1. Top: the AR strength scale from Ralph et al. (2019) based on maximum instantaneous IVT magnitude and duration of AR conditions (i.e., IVT $\geq$ 250 kg m^{-1}s^{-1}). Bottom: an AR precipitation impact scale based on mean precipitation rate (MPR) and duration of AR conditions.

Max IVT (kg m^{-1}s^{-1})	Duration (h) of AR conditions (IVT $\geq$ 250 kg m^{-1}s^{-1})		
	$\leq$ 24	$\geq$ 24–48	$\geq$ 48
$<$ 250	Not an AR	Not an AR	Not an AR
$\geq$ 250–500	Negligible AR (S0)	Weak AR (S1)	Moderate AR (S2)
$\geq$ 500–750	Weak AR (S1)	Moderate AR (S2)	Strong AR (S3)
$\geq$ 750–1000	Moderate AR (S2)	Strong AR (S3)	Extreme AR (S4)
$\geq$ 1000–1250	Strong AR (S3)	Extreme AR (S4)	Exceptional AR (S5)
$\geq$ 1250	Extreme AR (S4)	Exceptional AR (S5)	Exceptional AR (S5)
MPR (mm/24h)	**Duration (h) of AR conditions (IVT $\geq$ 250 kg m^{-1}s^{-1})**		
	$\leq$ 24	$\geq$ 24–48	$\geq$ 48
$<$ 25	Negligible impact (P0)	Negligible impact (P0)	Negligible impact (P0)
$\geq$ 25–50	Marginal impact (P0)	Weak impact (P1)	Moderate impact (P2)
$\geq$ 50–75	Weak impact (P1)	Moderate impact (P2)	Strong impact (P3)
$\geq$ 75–100	Moderate impact (P2)	Strong impact (P3)	Extreme impact (P4)
$\geq$ 100–150	Strong impact (P3)	Extreme impact (P4)	Exceptional impact (P5)
$\geq$ 150	Extreme impact (P4)	Exceptional impact (P5)	Exceptional impact (P5)

(S4P0) at Sandspit, and an extreme AR with strong impact (S4P3) at Prince Rupert.

Our verification indicates that the GDPS model underforecast precipitation at Sandspit. The observed amount at this station is 41 mm over the 66h period ending at 0000 UTC 17 August, which is equivalent to an MPR of 14.9 mm (24h)$^{-1}$ (double of the predicted value). On the other hand, the forecast for Prince Rupert verified well. The observed amount at this station is 138 mm over the 60h ending at 1800 UTC 16 August, which translates into an MPR of 55.2 mm (24h)$^{-1}$. The torrential downpours caused flash flooding and landslides in the Prince Rupert area, leaving mud, silt, and debris on some highway sections; a landslide that occurred about 42 km east of the city on 16 August forced the emergency evacuation of at least 13 people (Millar, 2020).

It should be emphasized that this simple scale may work well along the coastal areas, but would not apply to inland regions where such MPRs cannot be achieved. It could be possible to locally adjust the MPR criteria based on local hydro-climatic conditions, or replace the MPR criteria with something else (e.g., the return period of precipitation intensity). These considerations, however, are beyond the scope of this study.

As shown in Fig. 15, the MPR values calculated from the FPR and PCR are very close; for the two examples, the PCR-based values are slightly higher than the FPR-based values. From an operational meteorologist's perspective, it may not be necessary to analyze the PCR, given that the FPR is almost always available in a modern operational weather forecast environment. Nevertheless, analyzing the PCR distribution can help forecasters better understand the contribution of horizontal water vapor convergence to heavy precipitation. In some scientific studies, when precipitation rate is not available in the dataset, PCR can be used as a proxy for estimated precipitation rate in storm classification analysis.

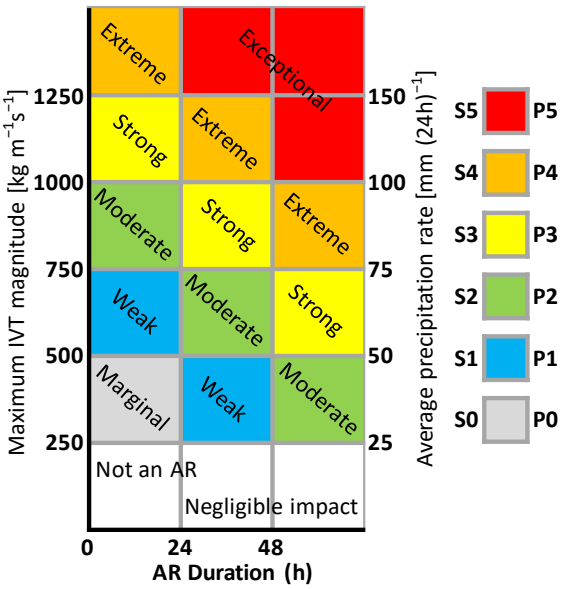

Figure 14. A combined scale that categorizes AR events based on the maximum IVT (left axis) as well as on the mean precipitation rate (MPR) over a period of AR conditions (IVT $\geq$ 250 kg m^{-1}s^{-1}) at a point. The combined scale is given in the format of SxPy, where "Sx" is the strength scale determined from the left axis (Ralph et al., 2019), and "Py" is the precipitation impact scale determined from the right axis. These two components are calculated independently over the same duration of AR conditions.

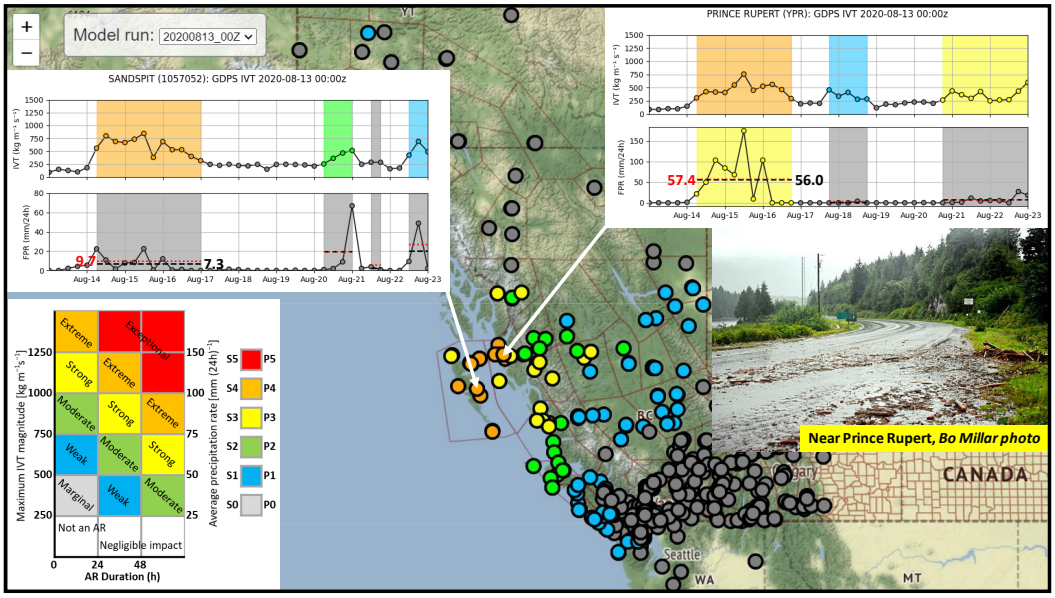

Figure 15. The predicted strength and impact scales of a mid-August AR over western Canada based on the GDPS operational forecast initialized at 0000 UTC 13 August 2020 and the proposal outlined in Table 1. The time series plots show IVT and FPR variations at Sandspit and Prince Rupert. The values of mean precipitation rate (MPR) calculated from the FPR and the PCR for each AR duration are indicated by the black dashed and red dotted lines, respectively. The embedded photo (courtesy of Bo Millar) shows dangerous road conditions near Prince Rupert after torrential rain caused flash flooding in the area (Millar, 2020).

6 Discussions and Conclusions

Heavy precipitation events, often in combination with snowmelt, can lead to numerous hazards, including flooding, washouts, river bank erosion, channel scour, landslides, and avalanches. These processes can lead to severe economic losses and fatalities where they intercept development and infrastructure. They can also cause major environmental damage, for example, through a landslide, or the severing of an oil pipeline. Hence, accurate storm prediction is of paramount importance even for remote communities.

The development of heavy and prolonged precipitation requires a sufficient supply of moisture and a physical mechanism to produce condensation. Atmospheric rivers, defined as long and narrow corridors of strong horizontal moisture transport, can provide such necessary conditions. A standard AR analysis usually involves calculating the IWV and IVT to identify the strength, location, and movement of the AR system. In this study, we propose the column relative humidity and the primary condensation rate as two supplements to the standard AR analysis to focus attention on the AR contribution to heavy precipitation. Both CRH and PCR are diagnosable variables. The CRH measures the relative moistness of the air column and the PCR can be used as a proxy measure of the large-scale precipitation rate.

The PCR is defined as a simple function of the CRH and the convergence of integrated horizontal water vapor flux. It is based on the concept that the converged vapor is shared between condensation and a general moistening of the air column. There are two empirically adjustable parameters in our proposed algorithm for PCR. Their optimal values are determined in this study based on a full year of NWP model data. Our case studies have shown that the diagnosed PCR can be used to correctly identify the location and strength of heavy precipitation associated with ARs. The location of heavy precipitation is not necessarily co-located with the maximum IVT, given that precipitation is directly associated with the net convergence rather than with the transfer of moisture. The moisture convergence in the lower atmosphere can be caused by orographic or frontal forcing, which usually also includes the physical mechanism to set up the vertical motions necessary to produce condensation and precipitation.

The precipitation efficiency also depends on the initial vertical distribution of water vapor in the air column, which is indicated by the CRH, and it can be expected that heavy precipitation is always associated with a large value of CRH. Our case studies showed that precipitation in the areas with CRH < 0.5 is negligible. In this study, the cut-off value of CRH for the PCR algorithm is 0.6.

The diagnosable PCR focuses attention on the primary factor leading to condensation: the horizontal water vapor transport and convergence. It can be used to represent the primary precipitation rate (PPR) if, and only if, condensed water storage in neglected. We have pointed out that in Eq. (5) the divergence of condensed water flux, $\nabla\cdot\mathbf{Q}_c$, can be at times as important as the convergence of vapor flux, $-\nabla\cdot\mathbf{Q}$. Under such circumstances, one can define $\mathrm{PPR} = (\mathrm{PCR} - \rho_w^{-1}\nabla\cdot\mathbf{Q}_c) \geq 0$. This is usually the case when an AR is blocked by a large mountain range. A fraction of the condensation over the windward slope will be carried by strong winds to the leeward side of the mountain, leading to the spillover phenomenon (e.g., Mo et al., 2019). To deal with this issue, one needs to estimate the vertical distribution of the specific condensed water q_c. This is sometimes challenging because it is much more difficult to measure q_c than q in the atmosphere, and some NWP model data (including reanalyses) only have q_c for cloud condensates.

In an operational forecast environment, the quantitative precipitation forecasts should be based on the FPR provided by the NWP model guidance rather than the less-accurate PCR. The added value of PCR is to help operational forecasters better understand the contribution of horizontal water vapor convergence to heavy precipitation. A potential

application of PCR or FPR in storm classification analysis is also discussed in this study. It is possible to add an impact component to the AR scale introduced by Ralph et al. (2019), so that an AR could be categorized using a combined scale in the format of "SxPy", where "Sx" is the scale based on its strength and duration (Ralph et al., 2019), and "Py" is the scale based on its precipitation impact calculated from the time average or integration of PCR or FPR. From a user perspective, the AR scale has to be simple enough that there is no confusion when it is communicated to the general public and decision makers. The scale introduced by Ralph et al. (2019) uses the intensity of IVT and AR event duration to characterize AR strength. It is simple and straightforward. When it is used as a proxy for estimated impact, the underlying assumption is that the IVT and the resulting precipitation rate are linearly correlated. Since precipitation is directly associated with the net moisture convergence rather than with the IVT, it would be useful, and perhaps necessary, to add a component such as the P-scale to explicitly address the AR impact on precipitation.

It is also possible to develop a multi-impact scale that includes several more hydroclimatic variables meant to be closer linked to the actual impacts of a storm. For example, the proposed SxPy scale does not include antecedent moisture which is known from several studies to be very important for landslide triggering and runoff (Jakob & Weatherly, 2003). Under certain circumstances, an AR could be classified as a strong or extreme (e.g., S4P4) storm, but it may lead to no or only few landslides and only minor flooding because tree canopies and the forest soil duff layer can absorb substantial volumes of moisture before it is released into the stream network or manifested as landslides. This is particularly important for short duration storms that do not allow overcoming of soil suction (negative pore water pressures) during the storm. For multi-day storms, and those occurring in the fall when preceding rains have partially saturated forest soils, the connection with heavy rain and landslides is more direct. In addition, landuse and forest state will affect the severity of a given storm in forested mountainous terrain. Areas with clearcuts and poorly constructed forest roads will be more susceptible to landslides and washouts compared to undisturbed terrain. Similarly, areas that have been burned by recent wildfires will respond more readily to heavy rain events. This means that for such areas, the impacts may be one category greater than suggested by Fig. 14. Lastly, the current scale does not include shorter duration precipitation (1 hour or less) which is known to be critical for landslide initiation, especially debris flows and debris avalanches (see Jakob & Owen, 2021). In short, moderate rainfall intensities ($< \sim 4\,\mathrm{mm\ h^{-1}}$) may not trigger such landslides as excess pore water pressures cannot develop. That said, many storms embed cells of high intensity rainfall as evidenced by weather radar echos. Development of a more comprehensive scale to address these issues is desirable, but it is beyond the scope of this paper.

Acknowledgments

Preliminary results from this study were presented at 2020 AGU Fall Meeting (Mo, 2020). We would like to thank Giselle Bramwell and Johnson Zhong (ECCC) for their help in precipitation and radar data collection, Bobby Sekhon (ECCC) for his weather briefing, and Brian Crenna (ECCC) for his assistance with the AR scale application development. Lin Xu and Chengzhi Ye (Hunan Meteorological Service, China) are acknowledged for their partial support of this study. We also thank Dr. Hai Lin (ECCC) for his internal review of this study.

Appendix A Specific Humidity and Saturation Specific Humidity

The specific humidity q is a useful quantity in meteorology. It is defined as the mass of water vapor in a unit of moist air. Its value can be either obtained from the NWP model

output or calculated from the following relations (Stull, 2017)

$$q = \epsilon e/[p - (1-\epsilon)e], \quad e = \rho_{\mathrm{v}} R_{\mathrm{v}} T, \tag{A1}$$

where e is the partial pressure due to water vapor (often known as vapor pressure), p is the total air pressure, $\epsilon = 0.622$ is a gas-constant ratio, ρ_{v} is the density of water vapor (absolute humidity), $R_{\mathrm{v}} = 461.5\ \mathrm{J\,K^{-1}kg^{-1}}$ is the gas constant for pure water vapor, and T is the absolute temperature (K).

The saturation specific humidity q_{s} is the specific humidity corresponding to the maximum amount of water vapor that can exist in air for a given temperature and pressure. It can be calculated using Eq. (A1) with e replaced by the saturation vapor pressure e_{s}. Alduchov and Eskridge (1996) recommended the following two equations to calculate e_{s} for moist air above a plane surface of liquid water (e_{sa}) or ice (e_{si}),

$$e_{\mathrm{sw}} = 6.11374 \exp[4.5 \times 10^{-6} p + 17.625 t/(t + 243.04)], \tag{A2}$$

$$e_{\mathrm{si}} = 6.10489 \exp[8 \times 10^{-6} p + 22.587 t/(t + 273.86)], \tag{A3}$$

where t is the temperature in Celsius degrees, and the pressure unit in these equations is hPa.

Given that supercooled liquid water can exist in the atmosphere with temperatures in the range $-40°\mathrm{C} < t < 0°\mathrm{C}$ (Stull, 2017), in this study we calculate e_{s} as a weighted average of e_{sw} and e_{si}, i.e.,

$$e_{\mathrm{s}} = a_{\mathrm{w}} e_{\mathrm{sw}} + (1 - a_{\mathrm{w}}) e_{\mathrm{si}}, \quad \text{with } a_{\mathrm{w}} = \begin{cases} 1, & \text{if } t > 0°\mathrm{C}, \\ (t+40)/40, & \text{if } -40°\mathrm{C} < t \le 0°\mathrm{C}, \\ 0, & \text{if } t \le -40°\mathrm{C}. \end{cases} \tag{A4}$$

Note that, with t replaced by the dewpoint t_{d}, the above equations can also be used to calculate the vapor pressure e.

References

Alduchov, O. A., & Eskridge, R. E. (1996). Improved Magnus form approximation of saturation vapor pressure. *J. Appl. Meteor.*, *35*, 601–609. doi: 10.1175/1520-0450(1996)035⟨0601:IMFAOS⟩2.0.CO;2

American Meteorological Society. (2021). *Glossary of Meteorology.* (Available online at `http://glossary.ametsoc.org/wiki/Atmospheric_river`)

Anthes, R. A. (1977). A cumulus parameterization scheme utilizing a one-dimensional cloud model. *Mon. Wea. Rev.*, *105*, 270–286. doi: 10.1175/1520-0493(1977)105⟨0270:ACPSUA⟩2.0.CO;2

Benton, G. S., & Estoque, M. A. (1954). Water-vapor transfer over the North American continent. *J. Meteor.*, *11*, 462–477. doi: 10.1175/1520-0469(1954)011⟨0462:WVTOTN⟩2.0.CO;2

Blamey, R. C., Ramos, A. M., Trigo, R. M., Tomé, R., & Reason, C. J. C. (2018). The influence of atmospheric rivers over the South Atlantic on winter rainfall in South Africa. *J. Hydrometeor.*, *19*, 127–142. doi: 10.1175/JHM-D-17-0111.1

Bretherton, C. S., Peters, M. E., & Back, L. E. (2004). Relationships between water vapor path and precipitation over the tropical oceans. *J. Climate*, *17*, 1517–1528. doi: 10.1175/1520-0442(2004)017⟨1517:RBWVPA⟩2.0.CO;2

Chen, J., Zhang, H., Ye, C., Chen, H., & Mo, R. (2020). Case studies of atmospheric rivers over China and Australia: new insight into their rainfall generation. *J. South. Hemisph. Earth Syst. Sci.*, *70*, 17–35. doi: 10.1071/ES19026

Cordeira, J. M., Ralph, F. M., & Moore, B. J. (2013). The development and evolution of two atmospheric rivers in proximity to western North Pacific

tropical cyclones in October 2010. *Mon. Wea. Rev.*, *141*, 4234–4255. doi: 10.1175/MWR-D-13-00019.1

Cruickshank, A. (2019). A river in the sky: Atmospheric rivers are changing. *Star Metro Vancouver*, 31 May, p.1 and p.6. (Available online at `https://projects.thestar.com/climate-change-canada/british-columbia/`)

Dettinger, M. (2004). *Fifty-Two Years of "Pineapple-Express" Storms across the West Coast of North America.* U.S. Geological Survey, Scripps Institution of Oceanography for the California Energy Commission, PIER Energy-Related Environmental Research. CEC-500-2005-004. (Available online at `http://www.energy.ca.gov/2005publications/CEC-500-2005-004/CEC-500-2005-004.PDF`)

Espy, J. P. (1841). *The Philosophy of Storms.* Boston, MA, USA: Charles C. Little and James Brown.

Garreaud, R. (2013). Warm winter storms in Central Chile. *J. Hydrometeor.*, *14*, 1515–1534. doi: 10.1175/JHM-D-12-0135.1

Guan, B., & Waliser, D. E. (2015). Detection of atmospheric rivers: Evaluation and application of an algorithm for global studies. *J. Geophys. Res. Atmos.*, *120*, 12514–12535. doi: 10.1002/2014GL060299

Hatchett, B. J., Cao, Q., Dawson, P. B., Ellis, C. J., Hecht, C. W., Kawzenuk, B., ... Sumargo, E. (2020). Observations of an extreme atmospheric river storm with a diverse sensor network. *Earth Space Sci.*, *6*, e2020EA001129. doi: 10.1029/2020EA001129

Houghton, H. G. (1951). On the physics of clouds and precipitation. In T. F. Malone (Ed.), *Compendium of meteorology* (pp. 165–181). Boston, MA, USA: Amer. Meteor. Soc. doi: 10.1007/978-1-940033-70-9_14

Huang, Z. (2020). Sichan floods lead to mass evacuation. *China Daily (Hong Kong Edition)*, 18 August, Page 4. (Available online at `https://www.chinadailyhk.com/epaper/pubs//chinadaily/2020/08/18/04.pdf`)

Jacob, D. (2001). The role of water vapour in the atmosphere. A short overview from a climate modeller's point of view. *Phys. Chem. Earth*, *26A*, 523–527. doi: 10.1016/S1464-1895(01)00094-1

Jakob, M., & Owen, T. (2021). Climate change effects on landslides in the North Shore Mountains of Vancouver. *Geomorphology*, In print.

Jakob, M., & Weatherly, H. (2003). A hydroclimatic threshold for landslide initiation on the North Shore Mountains of Vancouver, British Columbia. *Geomorphology*, *54*, 137–156. doi: 10.1016/S0169-555X(02)00339-2

Kuo, H.-L. (1974). Further studies of the parameterization of the influence of cumulus convection on large-scale flow. *J. Atmos. Sci.*, *31*, 1232–1240. doi: 10.1175/1520-0469(1974)031⟨1232:FSOTPO⟩2.0.CO;2

Lavers, D. A., Allan, R. P., Wood, E. F., Villarini, G., Brayshaw, D. J., & Wade, A. J. (2011). Winter floods in Britain are connected to atmospheric rivers. *Geophys. Res. Lett.*, *38*, L23803. doi: 10.1029/2011GL049783

Lavers, D. A., Villarini, G., Allan, R. P., Wood, E. F., & Wade, A. J. (2012). The detection of atmospheric rivers in atmospheric reanalyses and their links to British winter floods and the large-scale climatic circulation. *J. Geophys. Res. Atmos.*, *117*, D20106. doi: 10.1029/2012JD018027

Li, Y., Szeto, K., Stewart, R. E., Thériault, J. M., Chen, L., Kochtubajda, B., ... Kurkute, S. (2017). A numerical study of the June 2013 flood-producing extreme rainstorm over southern Alberta. *J. Hydrometeor.*, *18*, 2057–2078. doi: 10.1175/JHM-D-15-0176.1

Liu, A. Q., Mooney, C., Szeto, K., Thériault, J. M., Kochtubajda, B., Stewart, R. E., ... Pomeroy, J. (2016). The June 2013 Alberta catastrophic flooding event: Part 1–Climatological aspects and hydrometeorological features. *Hydrol. Process.*, *30*, 4899–4916. doi: 10.1002/hyp.10906

Lu, A. (1947). Precipitation in the South Chinese-Tibetan borderland. *Geog. Rev.*,

37, 88–93. doi: 10.2307/211363

Mahoney, K., Jackson, D. L., Neiman, P., Hughes, M., Darby, L., Wick, G., ... Cifelli, R. (2016). Understanding the role of atmospheric rivers in heavy precipitation in the Southeast United States. *Mon. Wea. Rev.*, *144*, 1617–1632. doi: 10.1175/MWR-D-15-0279.1

Manabe, S., & Wetherald, R. T. (1967). Thermal equilibrium of the atmosphere with a given distribution of relative humidity. *J. Atmos. Sci.*, *24*, 241–259. doi: 10.1175/1520-0469(1967)024⟨0241:TEOTAW⟩2.0.CO;2

Marshall, J. S., & Palmer, W. M. (1948). The distribution of raindrops with size. *J. Meteor.*, *5*, 165–166. doi: 10.1175/1520-0469(1948)005⟨0165:TDORWS⟩2.0.CO;2

McEwen, G. F. (1930). Our rainfall: how is it formed and what becomes of it? *Sci. Monthly*, *31*, 385–400. doi: 10.2307/15005

McTaggart-Cowan, R., Vaillancourt, P. A., Zadra, A., Chamberland, S., Charron, M., Corvec, S., ... Yang, J. (2019). Modernization of atmospheric physics parameterization in Canadian NWP. *J. Adv. Model. Earth Syst.*, *11*, 3593–3635. doi: 10.1029/2019MS001781

Millar, K.-J. (2020). "Don't put away your rain gear": Environment Canada. *Prince Rupert Northern View*, *14*, 20 August, A3. (Also see on A2: Dozens stranded after landslides block roads into Work Channel site; available online at `https://www.thenorthernview.com/e-editions/?pub_code=pru&&container=p20110819100700000&&date=2020-08`)

Mo, R. (2020). Diagnosing primary condensation rate attributed to the moisture convergence: Applications to atmospheric river analysis and extratropical storm classification. A117-0004, presented at 2020 Fall Meeting, AGU, 1-17 December. doi: 10.1002/essoar.10505440.1

Mo, R., Brugman, M. M., Milbrandt, J. A., Goosen, J., Geng, Q., Emond, C., ... Erfani, A. (2019). Impacts of hydrometeor drift on orographic precipitation: Two case studies of landfalling atmospheric rivers in British Columbia, Canada. *Wea. Forecasting*, *34*, 1211–1237. doi: 10.1175/WAF-D-18-0176.1

Mo, R., & Lin, H. (2019). Tropical–mid-latitude interactions: Case study of an inland-penetrating atmospheric river during a major winter storm over North America. *Atmos.-Ocean*, *57*, 208–232. doi: 10.1080/07055900.2019.1617673

National Weather Service. (2020). *Summary of August 14, 2020 severe weather event* (Tech. Rep.). Twin Cities, MN, USA: NWS, NOAA. (Available online at `https://www.weather.gov/mpx/August_14_2020_Severe_Weather_Event`)

Neiman, P. J., Ralph, F. M., Wick, G. A., Lundquist, J. D., & Dettinger, M. D. (2008). Meteorological characteristics and overland precipitation impacts of atmospheric rivers affecting the west coast of North America based on eight years of SSM/I satellite observations. *J. Hydrometeor.*, *9*, 22–47. doi: 10.1175/2007JHM855.1

Newell, R. E., Newell, N. E., Zhu, Y., & Scott, C. (1992). Tropospheric rivers? – A pilot study. *Geophys. Res. Lett.*, *19*, 2401–2404. doi: 10.1029/92GL02916

Paltan, H., Waliser, D., Lim, W. H., Guan, B., Yamazaki, D., Pant, R., & Dadson, S. (2017). Global floods and water availability driven by atmospheric rivers. *Geophys. Res. Lett.*, *44*. doi: 10.1002/2017GL074882

Pan, M., & Lu, M. (2019). A novel atmospheric river identification algorithm. *Water Resour. Res.*, *55*, 6069–6087. doi: 10.1029/2018WR024407

Peixoto, J. P. (1973). *Atmospheric Vapour Flux Computations for Hydrological Purposes*. Geneva, Switzerland: World Meteorological Organization.

Ralph, F. M., Neiman, P. J., & Wick, G. A. (2004). Satellite and CALJET aircraft observations of atmospheric rivers over the eastern North Pacific Ocean during the winter of 1997/98. *Mon. Wea. Rev.*, *132*, 1721–1745. doi: 10.1175/1520-0493(2004)132⟨1721:SACAOO⟩2.0.CO;2

Ralph, F. M., Rutz, J. J., Cordeira, J. M., Dettinger, M., Anderson, M., Reynolds,

D., ... Smallcomb, C. (2019). A scale to characterize the strength and impacts of atmospheric rivers. *Bull. Amer. Meteor. Soc.*, *100*, 269–289. doi: 10.1175/BAMS-D-18-0023.1

Rutz, J. J., Steenburgh, W. J., & Ralph, F. M. (2014). Climatological characteristics of atmospheric rivers and their inland penetration over the western United States. *Mon. Wea. Rev.*, *142*, 905–921. doi: 10.1175/MWR-D-13-00168.1

Schneider, T., O'Gorman, P. A., & Levine, X. J. (2010). Water vapor and the dynamics of climate changes. *Rev. Geophys.*, *48*, RG3001. doi: 10.1029/2009RG000302

Sharma, A. R., & Déry, S. J. (2020). Contribution of atmospheric rivers to annual, seasonal, and extreme precipitation across British Columbia and southeastern Alaska. *J. Geophys. Res. Atmos.*, *125*(9), e2019JD031823. doi: 10.1029/2019JD031823

Shih, G. (2020). Floods devastate China's Yangtze basin as army mobilizes massive relief effort. *The Washington Post*, 22 August, Page A14. (Available online at `https://www.washingtonpost.com/world/asia_pacific/china-floods-emergency-rescue-military-sichuan-economy/2020/08/21/668ed212-e35b-11ea-82d8-5e55d47e90ca_story.html`)

Starr, V. P., & Peixoto, J. P. (1958). On the global balance of water vapor and the hydrology of deserts. *Tellus*, *10*, 188–194. doi: 10.1111/j.2153-3490.1958.tb02004.x

Stohl, A., & James, P. (2004). A Lagrangian analysis of the atmospheric branch of the global water cycle. Part I: Method description, validation, and demonstration for the August 2002 flooding in central Europe. *J. Hydrometeor.*, *5*, 656–678. doi: 10.1175/1525-7541(2004)005⟨0656:ALAOTA⟩2.0.CO;2

Stull, R. (2017). *Practical Meteorology: An Algebra-based Survey of Atmospheric Science*. Vancouver, BC, Canada: University of British Columbia. (Available online at `https://www.eoas.ubc.ca/books/Practical_Meteorology/`)

Sundqvist, H. (1978). A parameterization scheme for non-convective condensation including prediction of cloud water content. *Quart. J. R. Met. Soc.*, *104*, 677–690. doi: 10.1002/qj.49710444110

Sundqvist, H., Berge, E., & Kristjánsson, J. E. (1989). Condensation and cloud parameterization studies with a mesoscale numerical weather prediction model. *Mon. Wea. Rev.*, *117*, 1641–1657. doi: 10.1175/1520-0493(1989)117⟨1641:CACPSW⟩2.0.CO;2

Tan, Y., & Li, H. (2020). Chongqing flooding considered among worst city has ever seen. *China Daily (Hong Kong Edition)*, 21 August, Page 3. (Available online at `https://www.chinadailyhk.com/epaper/pubs//chinadaily/2020/08/21/03.pdf`)

Trenberth, K. E., & Guillemot, C. J. (1998). Evaluation of the atmospheric moisture and hydrological cycle in the NCEP/NCAR reanalyses. *Clim. Dyn.*, *14*, 213–231. doi: 10.1007/s003820050219

Tuller, S. E. (1971). The world distribution of annual precipitation efficiency. *J. Geography*, *70*, 219–223. doi: 10.1080/00221347108981623

Tuller, S. E. (1973). Seasonal and annual precipitation efficiency in Canada. *Atmosphere*, *11*, 52–66. doi: 10.1080/00046973.1973.9648348

Tyndall, J. (1863). On radiation through the earth's atmosphere. *London Edinburgh Dublin Philos. Mag. J. Sci.*, *25*, 200-206. doi: 10.1080/14786446308643443

Wick, G. A., Neiman, P. J., & Ralph, F. M. (2013). Description and validation of an automated objective technique for identification and characterization of the integrated water vapor signature of atmospheric rivers. *IEEE Trans. Geosci. Remote Sens.*, *51*, 2166–2176. doi: 10.1109/TGRS.2012.2211024

Xiong, Y., & Ren, X. (2021). Influences of atmospheric rivers on North Pacific winter precipitation: Climatology and dependence on ENSO condition. *J. Climate*, *34*, 277–292. doi: 10.1175/JCLI-D-20-0301.1

Ye, C., Zhang, H., Moise, A., & Mo, R. (2020). Atmospheric rivers in the Australia-Asian region: a BoM-CMA collaborative study. *J. South. Hemisph. Earth Syst. Sci.*, *70*, 3–16. doi: 10.1071/ES19025

Zhang, Z., Ralph, F. M., & Zheng, M. (2019). The relationship between extratropical cyclone strength and atmospheric river intensity and position. *Geophys. Res. Lett.*, *46*, 1814–1823. doi: 10.1029/2018GL079071

Zhao, M. (2020). Simulations of atmospheric rivers, their variability, and response to global warming using GFDL's new high-resolution general circulation model. *J. Climate*, *33*, 10287–10303. doi: 10.1175/JCLI-D-20-0241.1

Zhu, Y., & Newell, R. E. (1994). Atmospheric rivers and bombs. *Geophys. Res. Lett.*, *21*, 1999–2002. doi: 10.1029/94GL01710

Zhu, Y., & Newell, R. E. (1998). A proposed algorithm for moisture fluxes from atmospheric rivers. *Mon. Wea. Rev.*, *126*, 725–735. doi: 10.1175/1520-0493(1998)126⟨0725:APAFMF⟩2.0.CO;2